Stress-Induced Quadrupole Splittings of Li^7 NMR in KCl:Li^+ †

D. W. ALDERMAN* AND R. M. COTTS
Laboratory of Atomic and Solid State Physics, Cornell University, Ithaca, New York 14850
(Received 4 December 1969)

Measurements of stress-induced first-order electric quadrupole splittings of the Li^7 NMR line in KCl:Li^+ are reported for the temperature range 1.3 to 4.2 K. Data are presented for uniaxial stresses up to −287 bar applied parallel to [001], [110], and [111] with the magnetic field rotated in the plane perpendicular to the stress. No splitting is observed for stress parallel to [001]. For stress parallel to [110], a splitting proportional to $\sin^2\beta$ is observed, where β is the angle between the magnetic field and [001]. A splitting independent of magnetic field direction is observed for stress parallel to [111]. Data for the temperature and stress dependence of the quadrupole splitting with stress parallel to [110] and the magnetic field parallel to [1$\bar{1}$0] are presented. The splittings are consistent only with the ⟨111⟩ or XY_8 model of the Li^+ impurity site. By fitting the temperature and stress dependence data with a linear combination of atomic orbitals (LCAO) tunneling model a value of $e^2Q/h=71\pm3$ kHz is obtained for the quadrupole interaction of a nucleus localized in one well. The fit also quantitatively determines the response of the impurity site to stress.

I. INTRODUCTION

WHEN KCl is doped with LiCl, Li^+ ions substitute for K^+ ions in the KCl lattice. Such crystals, designated KCl:Li^+, were first reported to have unusual properties by Baumann,[1] who noted a decrease in their thermal conductivity between 0.5 and 1.0 K indicating the presence of low-lying resonant states. Sack and Moriarty[2] reported that the monatomic Li^+ impurity behaved like a relaxation oriented electric dipole and Lombardo and Pohl[3] observed an electrocaloric effect. To explain these results Lombardo and Pohl[3] proposed that the Li^+ ion moved in a multiple well potential which had a maximum at the center of the impurity site and minima off center. The low-lying states are then tunneling states and the dipole behavior arises from the easy displacement of the positively charged Li^+ ion from the center of the negative charge surrounding the site. Matthew[4] showed that polarization forces can give rise to such off-center potential minima. A calculation by Dienes, Hatcher, Smoluchowski, and Wilson[5] showed minima in the potential as a function of distance along the ⟨001⟩ directions. Bowen, Gomez, Krumhansl, and Matthew[6] noted that there are three possibilities for the well minima locations consistent with the cubic symmetry of the site: There may be six minima along the ⟨001⟩ directions, eight minima along the ⟨111⟩ directions, or 12 minima along the ⟨110⟩ directions. These three possibilities are designated the XY_6, XY_8, and XY_{12} models, respectively. Calculating the energy levels for the XY_8 model with a linear combination of atomic orbitals (LCAO) approximation including edge overlap integrals, Bowen, Gomez, Krumhansl, and Matthew[6] found four equally spaced levels with degeneracies 1:3:3:1. Byer and Sack[7] showed with ultrasonic velocity measurements that the XY_8 model is appropriate. Lakatos and Sack[8] measured the spacing between adjacent levels as approximately 0.81 cm^{-1} with a microwave absorption experiment. Absolute minima in the ⟨111⟩ directions were then found by calculation by Quigley and Das[9] and by Wilson, Hatcher, Dienes, and Smoluchowski.[10] Specific-heat measurements by Harrison, Peressini, and Pohl[11] also confirm the ⟨111⟩ model and give 0.82 cm^{-1} as the Li^7 impurity level spacing.

The purpose of this work is to provide an independent check of the Gomez, Bowen, and Krumhansl (GBK)[6] XY_6 model. The experiment consists in measuring the uniaxial stress induced electric quadrupole splittings of the Li^7 nuclear magnetic resonance (NMR) line at liquid-helium temperatures. NMR bears on the problem because nuclear electric quadrupole moments couple to the electric field gradients (EFG's) present at points which lack cubic symmetry; in particular, the electric quadrupole moment of the spin-$\frac{3}{2}$ Li^7 nucleus couples to the EFG present when the Li^+ ion is off center. The nature of the EFG depends on the location of the well minima; thus the XY_6, XY_8, and XY_{12} models can be

† Work supported in part by the Advanced Research Projects Agency through the Materials Science Center at Cornell, MSC Report No. 1257, and by the National Science Foundation through Grant No. GP-9343. Based in part on the thesis submitted by one of the authors (D. W. A.) in partial fulfillment of the Ph.D. degree, Cornell University, 1969 (unpublished).
* National Science Foundation Predoctoral Fellow. Present address: National Bureau of Standards, Boulder, Colo. 80302.
[1] F. C. Baumann, Bull. Am. Phys. Soc. **9**, 644 (1964); F. C. Baumann, J. P. Harrison, R. O. Pohl, and W. D. Seward, Phys. Rev. **159**, 691 (1967).
[2] H. S. Sack and M. C. Moriarty, Solid State Commun. **3**, 93 (1965).
[3] G. Lombardo and R. O. Pohl, Phys. Rev. Letters **15**, 291 (1965).
[4] J. A. D. Matthew, Solid State Commun. **3**, 365 (1965).
[5] G. J. Dienes, R. D. Hatcher, R. Smoluchowski, and W. Wilson, Phys. Rev. Letters **16**, 25 (1966).
[6] S. P. Bowen, M. Gomez, J. A. Krumhansl, and J. A. D. Matthew, Phys. Rev. Letters **16**, 1105 (1966); M. Gomez, S. P. Bowen, and J. A. Krumhansl, Phys. Rev. **153**, 1009 (1967).
[7] N. E. Byer and H. S. Sack, Phys. Rev. Letters **17**, 72 (1966); N. E. Byer and H. S. Sack, J. Phys. Chem. Solids **29**, 667 (1968).
[8] A. Lakatos and H. S. Sack, Solid State Commun. **4**, 315 (1966).
[9] R. J. Quigley and T. P. Das, Solid State Commun. **5**, 487 (1967); R. J. Quigley and T. P. Das, Phys. Rev. **164**, 1185 (1967).
[10] W. D. Wilson, R. D. Hatcher, G. J. Dienes, and R. Smoluchowski, Phys. Rev. **161**, 888 (1967).
[11] J. P. Harrison, P. P. Peressini, and R. O. Pohl, Phys. Rev. **171**, 1037 (1968).

distinguished by determining the EFG. This can be done by applying a magnetic field which couples to the magnetic dipole moment of the nucleus and observing resonant frequencies as a function of magnetic field direction. In this work the energy associated with the electric quadrupole interaction is much smaller than that of the magnetic dipole interaction and thus can be treated as a first-order perturbation which gives rise to a splitting of the magnetic resonance line.

A complication is the fact that the Li^+ ion cannot be localized in one well. In fact, in the absence of externally applied stress or electric fields, the Li^+ ion spends an equal fraction of time in each well; there is thus net cubic symmetry so that the EFG vanishes and the quadrupole splitting is zero. As a consequence it is necessary to perturb the impurity to observe quadrupole splittings; the perturbation used here is uniaxial stress. Stress changes the fraction of time the ion spends in each well and thus produces an effect similar to that of localizing the ion in one well.

This paper is organized as follows: Section II describes briefly the sample preparation and experimental techniques used. Section III presents the results of measurements of stress induced quadrupole splittings as a function of magnetic field orientation and stress orientation. Also included in Sec. III are measurements of quadrupole splittings as a function of temperature and stress magnitude. In Sec. IV the theory is presented and the data are interpreted: Section IV A reviews spin-$\frac{3}{2}$ first-order quadrupole splittings and relevant motional averaging arguments. Section IV B reviews the GBK model. Section IV C extracts the parameters necessary to the NMR theory from the GBK model and fits the data. The XY_8 model is found to be appropriate. The response of the impurity to stress and the strength of the off-center EFG are determined. Section V discusses the experiment's relation to past and future work.

II. EXPERIMENTAL DETAILS

Samples were cut from KCl:Li^+ crystals grown by Kryopolous seed pulling from a melt of 0.3 mole % LiCl into a chlorine-argon atmosphere; starting materials were Mallinkrodt A. R. grade powdered KCl and LiCl treated with chlorine.[12] The Li content of the crystals was measured with flame-emission photometry and found to be between 0.005 and 0.010 mole % LiCl.[13] In order to avoid the precipitation problems mentioned by Byer and Sack[7] the samples were annealed in a vacuum for at least 24 h at 400°C then cooled to room temperature in 4 h; immediately thereafter the sample was cooled to liquid-helium temperature and the experiment carried out. If the sample subsequently spent more than one day above liquid-nitrogen temperature it was reannealed.

[12] Cornell Materials Science Center Crystal Growing Facility.
[13] Cornell Materials Science Center Analytical Facility.

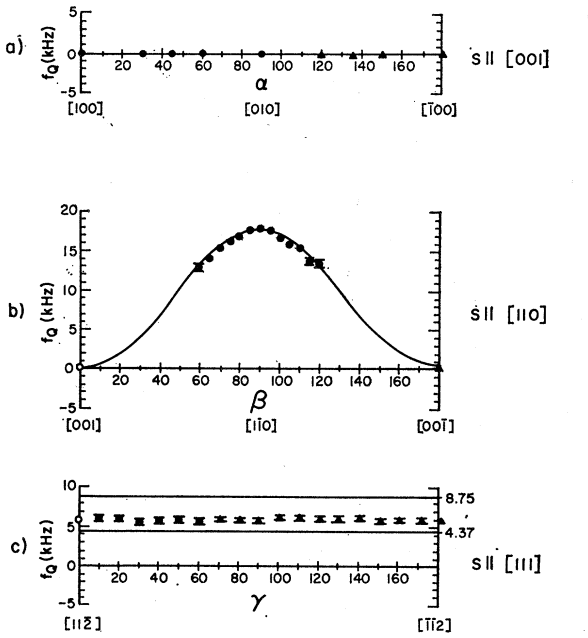

FIG. 1. Quadrupole splitting frequencies f_Q as a function of magnetic field orientation for $T=1.30$ K and $S=-287$ bars with (a) S∥[001], (b) S∥[110], and (c) S∥[111]. The dots are actual data; the triangles Δ are derived from the data by symmetry. Error bars are omitted where they are smaller than the datum symbols. Lines and curve are derived in Sec. III.

Samples were cylinders $\frac{3}{8}$ in. diameter by $\frac{1}{2}$ in. long. The axis of the cylindrical was oriented either along the [001], [110], or [111] crystal direction. The end faces of the sample were carefully ground parallel to one another. Force produced by a gas pressurized bellows was applied to the parallel ends of the sample through Teflon-faced anvils; this produced a uniform uniaxial stress parallel to the axis of the cylinder. No hysteresis was observed in the apparatus.

The temperature of the sample was controlled by direct immersion in a pumped liquid-helium bath.

The Li^7 cw NMR signal was observed at 16 MHz using a high-sensitivity spectrometer which employs a twin T bridge-MOSFET amplifier circuit immersed in the liquid-helium bath for signal-to-noise ratio improvement.[14] The magnetic field was provided by a Varian 12-in. electromagnet system fitted with the Varian Fieldial. Conventional field modulation lock-in detection at 100 Hz was used to obtain an approximation of the derivative of the absorption signal which was plotted on the Y axis of an XY recorder. The X axis of the recorder was driven by the Fieldial magnetic field sweep; this permitted registered display of multiple sweeps through the resonance line which proved to be a powerful and convenient method of signal to noise ratio enhancement.

The NMR coil was coaxial with the sample and the magnetic field $\mathbf{H}_0$ was perpendicular to the axis of the

[14] D. W. Alderman, Rev. Sci. Instr. 41, 192 (1970).

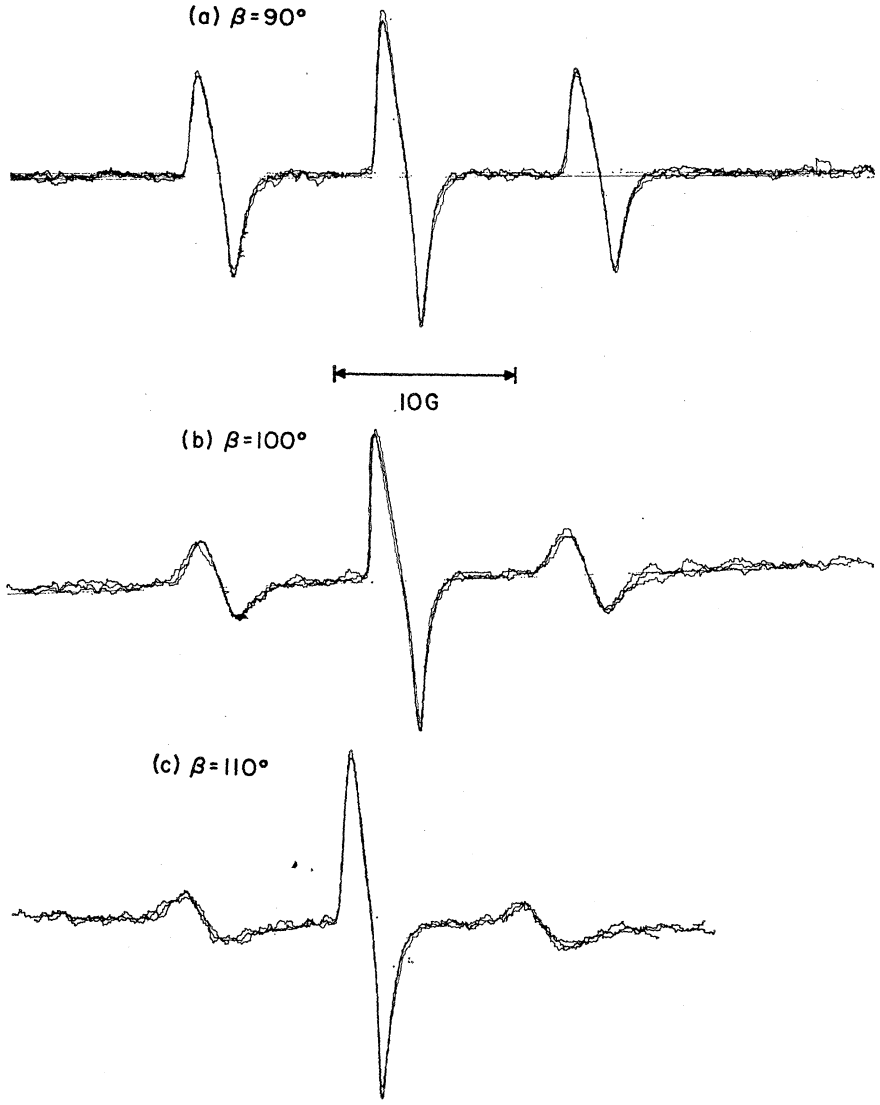

FIG. 2. Recorder plots of absorption first-derivative signals with S‖[110], $S=-287$ bars, $T=1.30$ K, and (a) $\beta=90°$, (b) $\beta=100°$, and (c) $\beta=110°$.

sample and the coil. The orientation of the magnetic field relative to the crystal was varied by rotating the sample about its cylindrical axis.

III. EXPERIMENTAL RESULTS

In the absence of applied stress the Li^7 NMR spectrum in KCl:Li^+ was a single line approximately 1 G wide. When uniaxial stress was applied in certain directions the line split in the manner characteristic of spin-$\frac{3}{2}$ first-order quadrupole interactions; the spectrum became an unshifted central line flanked by a symmetrical pair of sidebands. The quadrupole splitting frequency f_Q is defined as the difference between the frequencies of the central line and a sideband. Quadrupole splittings were reckoned as half the difference in magnetic field between the upper and lower sidebands as measured by the distance between the baseline crossings of the sidebands on the field swept derivative plot. Error bars were assigned to include the range of values obtained from from three to six sweeps through the line. Splittings in the magnetic field were converted to quadrupole splitting frequencies with the factor for Li^7: $\gamma/2\pi=1.6547$ kHz/G. In other circumstances uniaxial stress produced no detectable splitting; when this occurred the second moment of the line was calculated and the scatter in the values used as an estimate of the minimum detectable quadrupole splitting frequency.

Data were taken with uniaxial stress **S** parallel to the [001], [110], and [111] crystal directions, denoted S‖[001], S‖[110], and S‖[111], respectively. In each case the magnetic field $\mathbf{H}_0$ was rotated relative to the crystal in the plane perpendicular to the stress direction; the position of the magnetic field in this plane is defined as follows: For S‖[001], α is the angle between

$\mathbf{H}_0$ and [100]; for $\mathbf{S}\|[110]$, β is the angle between $\mathbf{H}_0$ and [001]; for $\mathbf{S}\|[111]$, γ is the angle between $\mathbf{H}_0$ and $[11\bar{2}]$.

With $\mathbf{S}\|[001]$ no splitting was observed. The line widths at $T=1.30$ K with magnetic field at $\alpha=0°$, 30°, 45°, 60°, and 90° for stress magnitudes, S, of 0, -70, -141, -218, and -287 bars were characterized by the line's second moment and derivative peak-to-peak width and peak-to-peak height. In no instance did the line broaden significantly by any of these criteria. Using the scatter in the second-moment data as a measure of a minimum detectable splitting frequency, the limit $f_Q<0.05$ kHz was placed on the quadrupole splitting frequency with $\mathbf{S}\|[001]$. The data are plotted in Fig. 1(a).

With $\mathbf{S}\|[110]$ quadrupole splitting was observed. Quadrupole splitting frequencies measured at $S=-287$ bars and $T=1.30$ K are plotted as a function of magnetic field orientation in Fig. 1(b). The splitting frequency reaches a maximum at $\beta=90°$, where $\mathbf{H}_0\|[1\bar{1}0]$. Figure 2 shows recorder plots from which three of the data points of Fig. 1(b) were taken. When $\beta=90°$ the sidebands have the same width as the central line; this width is caused by magnetic dipole broadening, and by finite $\mathbf{H}_0$ modulation and lock-in time constant. Away from $\beta=90°$, however, the sidebands are broader than the central line indicating the presence of inhomogeneous quadrupole broadening mechanisms. This increased width, which makes the sideband derivative intersection with the baseline less steep, is the cause of the larger error bars away from $\beta=90°$ in Fig. 1(b). The splitting frequency was not measured when the sidebands began to overlap the central line. The precise alignment of the magnetic field was accomplished by adjusting for minimum sideband width at $\beta=90°$. The splitting frequency at $\beta=0°$ was small; second-moment analysis similar to that used in the $\mathbf{S}\|[001]$ case showed that at $\beta=0°$ the quadrupole splitting frequency at $S=-287$ bar and $T=1.30$ K was less than 0.2 kHz.

The narrow sidebands at $\beta=90°$ afforded a unique opportunity to measure the stress and temperature dependence of the quadrupole splitting frequency. Such data are plotted in Fig. 3. The $\beta=90°$ sidebands which were narrow at $S=-287$ bar broadened as the stress was lowered giving rise to the larger error bars at low stresses in Fig. 3. Again the splitting frequency was not measured when the sidebands began to overlap the central line. The data shown are the best obtained. Other data consistently had larger sideband widths and smaller splittings.

The relative intensities of the central line and sidebands were measured with $\mathbf{S}\|[110]$ at $\beta=90°$, $T=1.30$ K and $S=-287$ bar and found to be within 0.01 of the theoretical values, 0.3:0.4:0.3 (see Sec. IV A), giving assurance that all of the quadrupole sidebands were being observed.

Also, at $\beta=90°$, $T=1.30$ K, and $\mathbf{S}\|[110]$ the second moment of the zero stress unsplit line and the second moment of the central line were measured with the sidebands removed by -287 bars of stress. The difference between the second moments of the unsplit line and the central line is 0.64 ± 0.10 kHz^2. The additional width of the unsplit line is caused by quadrupole interactions from residual strains in the crystal.

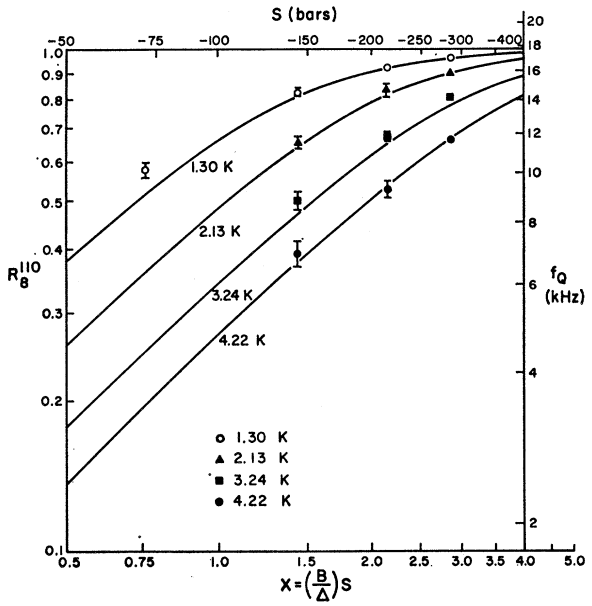

FIG. 3. Quadrupole splitting frequencies f_Q as a function of temperature and stress magnitude S with $\mathbf{S}\|[110]$ and $\beta=90°$. Error bars are omitted where they are smaller than the datum symbols. Upper and right scales apply to the data. Lower and left scales apply to the curves which are derived in Sec. III.

Quadrupole splitting was also observed with $\mathbf{S}\|[111]$. Quadrupole splitting frequencies as a function of magnetic field orientation observed at $S=-287$ bars and $T=1.30$ K are plotted in Fig. 1(c). Within the experimental uncertainty the splitting is independent of γ and is equal to 5.5 ± 0.5 kHz. This splitting is much smaller than those observed with $\mathbf{S}\|[110]$ and the sidebands are all broader than the central line. As a consequence, the sidebands are not well separated from the central line. This overlap pulls the sideband derivative intersections in, perhaps making the splitting given above too small. A maximum value, however, would be 6.5 kHz.

IV. THEORY AND INTERPRETATION

A. Nuclear Magnetic Resonance

The theory of nuclear magnetic dipole and electric quadrupole interactions is well developed.[15] The magneticdipole moment of a nucleus $\boldsymbol{\mu}=\hbar\gamma\mathbf{I}$ couples to an applied magnetic field $\mathbf{H}_0$ via an interaction described by the Zeeman Hamiltonian, $\mathcal{H}_Z=-\hbar\gamma\mathbf{I}\cdot\mathbf{H}_0$.

[15] A. Abragam, *The Principles of Nuclear Magnetism* (Oxford University Press, New York, 1961); C. P. Slichter, *Principles of Magnetic Resonance* (Harper and Row, New York, 1963).

The energy-level diagram of $\mathcal{H}_Z$ consists of $2I+1$ equally spaced levels which give rise to an absorption spectrum consisting of a single line at the frequency $f=(\gamma/2\pi)|\mathbf{H}_0|$.

The electric quadrupole moment of a nucleus eQ couples to the EFG at the nuclear site and adds another term $\mathcal{H}_Q$ to the Hamiltonian. $\mathcal{H}_Q$ is most conveniently described with the aid of a symmetric EFG tensor $\mathbf{V}$ whose components are the second partial spatial derivatives of the potential function: $\partial^2V/\partial x^2=V_{xx}$, $\partial^2V/\partial xy=V_{xy}$, etc. As for any symmetric tensor, a special set of coordinate axes, the principal axes, can be found in which the tensor is diagonal. Customarily the principal axes are labelled so that $|V_{zz}|\geq|V_{xx}|\geq|V_{yy}|$. Laplace's equation, $V_{xx}+V_{yy}+V_{zz}=0$, reduces the number of independent parameters from three to two; they are customarily taken as $eq=V_{zz}$ and $\eta=(V_{xx}-V_{yy})/V_{zz}$. If there is axial symmetry, the z principal axis will lie along the symmetry axis and the x and y principal axes are free to lie anywhere in the plane perpendicular to the symmetry axis; further, $V_{xx}=V_{yy}$ so that $\eta=0$. If there is cubic symmetry then $V_{xx}=V_{yy}=V_{zz}=0$ so that $eq=0$ and no quadrupole interaction exists. For a nucleus with spin $\frac{3}{2}$, such as Li^7, when the electric quadrupole interaction is small compared to the magnetic dipole interaction so that $\mathcal{H}_Q$ may be treated as a perturbation on $\mathcal{H}_Z$, the absorption spectrum consists of an unshifted central line at $f=(\gamma/2\pi)|\mathbf{H}_0|$ of relative intensity 0.4 and two sidebands each of relative intensity 0.3. The distance from the central line to a sideband is given by the quadrupole splitting frequency

$$f_Q=\tfrac{1}{4}(e^2Qq/h)(3\cos^2\theta-1+\eta\sin^2\theta\cos2\phi), \quad (1)$$

where θ and ϕ are the polar and azimuthal coordinates of the magnetic field direction in the principal axis coordinate system.

If the nucleus is stationary it experiences a static EFG and the situation is quite simple. If, on the other hand, the nucleus moves and experiences an EFG which is a function of its position $\mathbf{x}$ the effective EFG must be obtained from an average of the values of the local EFG's. In particular, if the motion of the nucleus is described by an eigenfunction $\Psi_\mu(\Gamma^\nu)(\mathbf{x})$ (the form of labeling the eigenfunctions will become more appropriate later), and the EFG tensor is $\mathbf{V}(\mathbf{x})$ when the nucleus is at $\mathbf{x}$, the eigenstate EFG tensor which determines f_Q is given by

$$\mathbf{V}_\mu(\Gamma^\nu)=\int\Psi_\mu(\Gamma^\nu)(\mathbf{x})^*\mathbf{V}(\mathbf{x})\Psi_\mu(\Gamma^\nu)(\mathbf{x})d^3x. \quad (2)$$

If the nuclear motion quantum system is in thermal equilibrium with a bath at temperature T so that a number of eigenstates are populated, two limiting cases may be treated. If the lifetimes of the eigenstates are very long compared to $1/f_Q$, then the nucleus experiences many different values of the EFG and a multisideband absorption spectrum results. If, on the other hand, the lifetimes are very short compared to $1/f_Q$, then transitions between states result in averaging over values of the EFG characteristic of each state. The resultant effective EFG tensor is a Boltzmann average of the eigenstate EFG tensors given by

$$\langle\mathbf{V}_\mu(\Gamma^\nu)\rangle=Z^{-1}\sum_\nu\exp(-E(\Gamma^\nu)/kT)\mathbf{V}_\mu(\Gamma^\nu), \quad (3)$$

where $Z=\sum_\nu e^{-E(\Gamma^\nu)/kT}$. The position of the single set of sidebands is now calculated by diagonalizing this average tensor and then applying Eq. (1).

In the long-lifetime case, the sideband intensity will be shared among the sidebands corresponding to different eigenstates. In the short-lifetime case, however, all the sideband intensity is in one sideband and the 0.3:0.4:0.3 intensity ratio applies. Since the data exhibit 0.3:0.4:0.3 intensity ratios the short-lifetime calculation is appropriate.

B. LCAO Model

The GBK theory[6] provides a framework within which the averages of Eqs. (2) and (3) may be evaluated for KCl:Li^+. GBK's calculation is a quantum-mechanical treatment of the motion of a single Li ion, i.e., the ion nuclear mass, in the KCl lattice. They write a lattice Hamiltonian, $\mathcal{H}=\mathcal{H}_L+\mathcal{H}_I+\mathcal{H}_C$, where $\mathcal{H}_L$ includes only K and Cl ion momenta and positions, $\mathcal{H}_I$ includes only the Li impurity ion momentum and position, and $\mathcal{H}_C$ includes terms which contain mixtures of K, Cl, and Li positions. After showing that $\mathcal{H}_I$ is the Hamiltonian of the Li ion motion if the host lattice ions are constrained to their equilibrium positions, they turn to the approximation of its low-lying eigenstates and energies. Their method is the LCAO approximation, a variational calculation scheme in which the variational parameters are coefficients in linear combinations of a finite number of suitably chosen basis states. The equivalence of the variational extremal problem and the linear operator eigenvalue problem makes the calculation identical to those of matrix quantum mechanics in a finite dimensional state space. Energies and coefficients in eigenstate linear combinations are found by diagonalizing matrices representing the Hamiltonian in a restricted state space.

GBK treat three models of potentials with off-center minima which they designate XY_6, XY_8, and XY_{12}. Schematic representations showing potential-minima locations for the three models are shown in Fig. 4. The XY_6 model potential has six minima displaced from the impurity site center in the ⟨001⟩ directions. The XY_8 model potential has eight minima displaced in the ⟨111⟩ directions. The XY_{12} model potential has twelve minima displaced in the ⟨110⟩ directions. The difference in the treatment of the three models consists in the choice of basis states for the LCAO calculation.

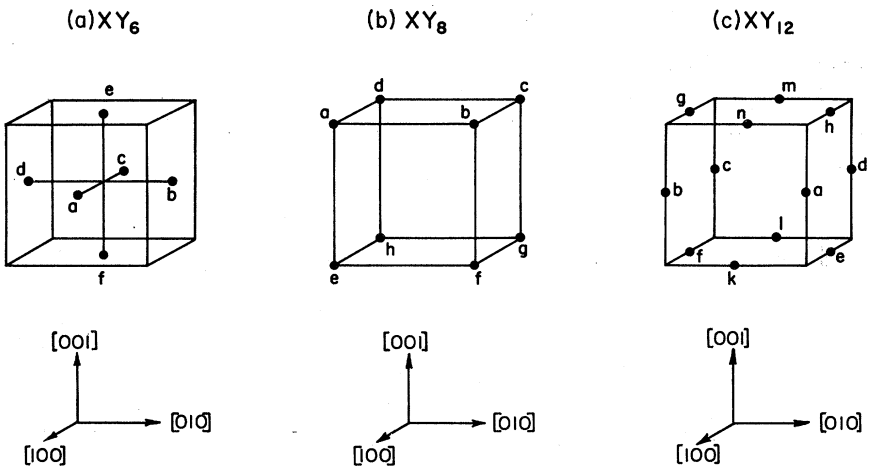

FIG. 4. Schematic representation of locations of potential-well minima in XY_6, XY_8, and XY_{12} models.

For each model, basis states are chosen each of which has significant amplitude only in the volume associated with one potential minimum. Thus, for example, the basis states for the XY_8 calculation are eight functions, $\psi_a, \psi_b, \ldots \psi_h$, each of which is large only in the corresponding octant of Fig. 4(b). The Hamiltonian can then be diagonalized with the group theory of the octahedral (O_h) symmetry of the site. The eigenstates, which are labeled by their transformation properties, are linear combinations of the basis states ψ_n written

$$\Psi_\mu(\Gamma^\nu)=\sum_n c_{n\mu}(\Gamma^\nu)\psi_n. \tag{4}$$

The energies of the eigenstates depend upon the nature of the overlap integrals between basis states. The GBK calculation method is appropriate when these overlap integrals are small.

The results of the GBK calculation are approximate eigenstates and energies for only the low-lying states of the impurity Hamiltonian $\mathcal{H}_I$; it does not concern itself with higher states.

C. Application to KCl:Li$^+$

These preliminaries provide some insight into the averages of Eqs. (2) and (3). Inserting Eqs. (2) and (4) into Eq. (3) yields

$$\langle \mathbf{V}_\mu(\Gamma^\nu)\rangle = Z^{-1}\sum_{\mu,\nu}\exp[-E(\Gamma^\nu)/kT]\mathbf{V}_\mu(\Gamma^\nu)$$

$$= Z^{-1}\sum_{\mu,\nu}\exp[-E(\Gamma^\nu)/kT]\int[\sum_m c_{m\mu}{}^*(\Gamma^\nu)\psi_m{}^*(\mathbf{x})]$$

$$\times\mathbf{V}(\mathbf{x})[\sum_n c_{n\mu}(\Gamma^\nu)\psi_n(\mathbf{x})]d^3\mathbf{x}.$$

Upon ignoring the cross terms, which are relatively small because the overlap integrals are small, the sums over m and n contract to a single sum yielding:

$$\langle \mathbf{V}_\mu(\Gamma^\nu)\rangle = Z^{-1}\sum_{\mu\nu}\exp[-E(\Gamma^\nu)/kT]$$

$$\times\sum_n |c_{n\mu}(\Gamma^\nu)|^2\int\psi_n{}^*(\mathbf{x})\mathbf{V}(x)\psi_n(\mathbf{x})d^3\mathbf{x}$$

$$=\sum_n\left(\sum_{\mu\nu}Z^{-1}\exp[-E(\Gamma^\nu)/kT]|c_{n\mu}(\Gamma^\nu)|^2\right)$$

$$\times\left(\int\psi_n{}^*(\mathbf{x})\mathbf{V}(\mathbf{x})\psi_n(\mathbf{x})d^3\mathbf{x}\right)=\sum_n p_n\mathbf{V}_n, \tag{5}$$

where

$$p_n=Z^{-1}\sum_{\mu\nu}\exp[-E(\Gamma^\nu)/kT]|c_{n\mu}(\Gamma^\nu)|^2 \tag{6}$$

and

$$\mathbf{V}_n=\int\psi_n{}^*(\mathbf{x})\mathbf{V}(\mathbf{x})\psi_n(\mathbf{x})d^3x. \tag{7}$$

The tensor $\mathbf{V}_n$ has simple symmetry properties. For example consider the XY_8 model: The symmetries of the wave function $\psi_a(\mathbf{x})$ and the tensor $\mathbf{V}(\mathbf{x})$ require that the tensor $\mathbf{V}_a$ describe an EFG with axial symmetry around [111]. Thus $\mathbf{V}_a$ is completely specified by one parameter eq_8. The rest of the $\mathbf{V}_n$ for the XY_8 model are derived by similar arguments; they have different principal axes but share the same parameter eq_8. Similar results apply to the XY_6 and XY_{12} models, though the $\mathbf{V}_n$ of the XY_{12} model need not have axial symmetry so that another parameter η_{12} is required. Calculation shows that for all the models $\Sigma_n\mathbf{V}_n=0$; this is a consequence of the net cubic symmetry of the impurity site.

The p_n also have simple properties; they are the thermal averages of the quantum mechanical probabilities for each basis state and thus normalization requires that $\Sigma_n p_n=1$. In the absence of any external perturbations, the impurity site has cubic symmetry and $p_n=1/N$, where N is the number of basis states,

TABLE I. Calculated stress-induced quadrupole splitting frequencies for the XY_6, XY_8, XY_{12}, and distortion models with S‖[001], S‖[110], and S‖[111].

Stress direction	XY_6	XY_8	XY_{12}	Distortion
S‖[001]	$f_Q=\frac{e^2Qq_6}{4h}R_6^{001}$	$f_Q=0$	$f_Q=\frac{e^2Qq_{12}}{4h}\frac{R_{12}^{001}}{2}(1-\eta_{12})$	$f_Q=-\frac{e^2Qq_d^{001}}{4h}$
S‖[110]	$f_Q=\frac{e^2Qq_6}{4h}R_6^{110}(3\cos^2\beta-1)$	$f_Q=\frac{e^2Qq_8}{4h}R_8^{110}(\sin^2\beta)$	$f_Q=\frac{e^2Qq_{12}}{4h}\left[\frac{{}_1R_{12}^{110}}{6}(3+\eta_{12})(\sin^2\beta)+\frac{{}_2R_{12}^{110}}{2}(1-\eta_{12})(3\cos^2\beta-1)\right]$	$f_Q=\frac{e^2Qq_d^{110}}{4h}(\eta\cos2\beta-1)$
S‖[111]	$f_Q=0$	$f_Q=\frac{e^2Qq_8}{4h}R_8^{111}$	$f_Q=\frac{e^2Qq_{12}}{4h}R_{12}^{111}(3+\eta_{12})$	$f_Q=-\frac{e^2Qq_d^{111}}{4h}$

6, 8, or 12 depending on the model. As a consequence, since $\langle\mathbf{V}_\mu(\Gamma^\nu)\rangle=\Sigma p_n\mathbf{V}_n=\Sigma(1/N)\mathbf{V}_n=(1/N)\Sigma\mathbf{V}_n=0$, the quadrupole splitting frequency is zero in the absence of stress or electric fields.

When external perturbations are applied, the effect is to modify the potential in which the Li^+ ion moves; the LCAO eigenstates and energies are thus perturbed and the thermal averages p_n are changed. If uniaxial stress is applied in a direction of high symmetry it is easy to see what the p_n do. For example, if stress is applied to the XY_8 model parallel to [001], the symmetry of the situation requires that all the p_n remain equal to $\frac{1}{8}$. Thus, if it is assumed that the $\mathbf{V}_n$ are unchanged by the application of stress, $\langle\mathbf{V}_\mu(\Gamma^\nu)\rangle$ remains zero and no quadrupole splitting is induced. If, on the other hand, stress is applied parallel to [110], the change in the p_n may be described by a single parameter as follows:

$$\begin{aligned}&p_a=p_c=p_e=p_g=\tfrac{1}{8}(1+R_8^{110}),\\&p_b=p_d=p_f=p_h=\tfrac{1}{8}(1-R_8^{110}),\end{aligned}\tag{8}$$

where R_8^{110} ranges from $+1$ to -1 and depends upon stress magnitude, temperature, and the response of the impurity site to stress. Evaluation of Eq. (5) now yields

$$\begin{aligned}\langle\mathbf{V}_\mu(\Gamma^\nu)\rangle&=\sum_n p_n\mathbf{V}_n=\sum_n\tfrac{1}{8}(1\pm R_8^{110})\mathbf{V}_n\\&=\sum_n\mathbf{V}_n+\tfrac{1}{8}\sum_n(\pm R_8^{110})\mathbf{V}_n\\&=\tfrac{1}{8}R_8^{110}(\mathbf{V}_a-\mathbf{V}_b+\mathbf{V}_c-\mathbf{V}_d+\mathbf{V}_e-\mathbf{V}_f+\mathbf{V}_g-\mathbf{V}_h).\end{aligned}$$

If again it is assumed that the $\mathbf{V}_n$ are unchanged by stress this equation immediately yields a nonzero net EFG tensor which may be diagonalized and used to predict quadrupole splittings.

Similar results are obtained for S‖[111]. Again the change in the p_n is described by a single parameter as follows:

$$\begin{aligned}&p_a=p_c=p_d=p_e=p_f=p_g=\tfrac{1}{8}(1+R_8^{111}),\\&p_b=p_h=\tfrac{1}{8}(1-3R_8^{111}),\end{aligned}\tag{9}$$

where R_8^{111} ranges from -1 to $+\frac{1}{3}$ and depends upon stress magnitude, temperature, and the response of the impurity site to stress in a way different from R_8^{110}. For this case Eq. (5) yields

$$\begin{aligned}\langle\mathbf{V}_\mu(\Gamma^\nu)\rangle=\tfrac{1}{8}R_8^{111}(&\mathbf{V}_a-3\mathbf{V}_b+\mathbf{V}_c\\&+\mathbf{V}_d+\mathbf{V}_e+\mathbf{V}_f+\mathbf{V}_g-3\mathbf{V}_h).\end{aligned}$$

The same procedure as above now yields predicted splittings for S‖[111]. The same sort of procedure is applicable to the XY_6 and XY_{12} models. The XY_{12} model is more complicated because two parameters, ${}_1R_{12}^{110}$ and ${}_2R_{12}^{110}$, are necessary to describe the change in the p_n when stress is applied parallel to [110].

The magnitude of the stress induced EFG tensors and thus electric quadrupole splitting frequencies

TABLE II. XY_8 model Hamiltonian matrices.

$$\mathcal{H}_I=\Delta\begin{pmatrix}-\frac{3}{2}&0&0&0&&&&&&&&\\0&\frac{1}{2}&0&0&&&&0&&&&\\0&0&\frac{1}{2}&0&&&&&&&&\\0&0&0&\frac{1}{2}&&&&&&&&\\&&&&-\frac{1}{2}&0&0&0&&&&\\&&&&0&-\frac{1}{2}&0&0&&&&\\&0&&&0&0&-\frac{1}{2}&0&&&&\\&&&&0&0&0&\frac{3}{2}&&&&\end{pmatrix}\begin{matrix}A_{1g}\\T_{2g}xy\\T_{2g}yz\\T_{2g}zx\\T_{1u}x\\T_{1u}y\\T_{1u}z\\A_{2u}\end{matrix}$$

$$\mathcal{H}_S^{110}=S\begin{pmatrix}0&B&0&0&&&&&&&&\\B&0&0&0&&&&0&&&&\\0&0&0&B&&&&&&&&\\0&0&B&0&&&&&&&&\\&&&&0&B&0&0&&&&\\&&&&B&0&0&0&&&&\\&0&&&0&0&0&B&&&&\\&&&&0&0&B&0&&&&\end{pmatrix}\begin{matrix}A_{1g}\\T_{2g}xy\\T_{2g}yz\\T_{2g}zx\\T_{1u}x\\T_{1u}y\\T_{1u}z\\A_{2u}\end{matrix}$$

$$\mathcal{H}_S^{111}=S\begin{pmatrix}0&\frac{2}{3}B&\frac{2}{3}B&\frac{2}{3}B&&&&&&&&\\\frac{2}{3}B&0&\frac{2}{3}B&\frac{2}{3}B&&&&0&&&&\\\frac{2}{3}B&\frac{2}{3}B&0&\frac{2}{3}B&&&&&&&&\\\frac{2}{3}B&\frac{2}{3}B&\frac{2}{3}B&0&&&&&&&&\\&&&&0&\frac{2}{3}B&\frac{2}{3}B&\frac{2}{3}B&&&&\\&&&&\frac{2}{3}B&0&\frac{2}{3}B&\frac{2}{3}B&&&&\\&0&&&\frac{2}{3}B&\frac{2}{3}B&0&\frac{2}{3}B&&&&\\&&&&\frac{2}{3}B&\frac{2}{3}B&\frac{2}{3}B&0&&&&\end{pmatrix}\begin{matrix}A_{1g}\\T_{2g}xy\\T_{2g}yz\\T_{2g}zx\\T_{1u}x\\T_{1u}y\\T_{1u}z\\A_{2u}\end{matrix}$$

depends on the unknown products $eq_8R_8^{110}$, $eq_8R_8^{111}$, $eq_6R_6^{110}$, etc. For a fixed temperature and direction and magnitude of stress, however, the EFG tensors remain constant and the splitting pattern as a function of magnetic field orientation may be calculated. Such results for the three models, XY_6, XY_8, and XY_{12}, for stress and magnetic field orientations corresponding to the experimental conditions are tabulated in Table I and sketched in Fig. 5.

The above calculations are of quadrupole splittings which arise because of a net EFG produced by stress induced relocation of the nucleus. Another possible source of EFG's is stress-induced distortion of the lattice, the nuclear position remaining the same. The splitting patterns that such a mechanism would produce in KCl:Li^+ if, for example, the Li^+ ion were on center and did not relocate, are shown in the fourth columns of Table I and Fig. 5. If both relocation and distortion mechanisms are at work the resultant quadrupole splitting patterns would be linear combinations of XY_6, XY_8, or XY_{12} splittings and distortion splittings.

Referring now to Figs. 1 and 5, note that in the absence of distortion effects the XY_8 model calculation is the only one consistent with the data. However, note that linear combinations of XY_6 or XY_{12} relocation and distortion splittings can also be made to fit the data; a cancellation of splittings can produce the null splitting observed with S‖[001]. Since the stress dependences of the XY_6 or XY_{12} splittings and the distortion splittings would be different, however, such a cancellation would occur only at a single stress magnitude. In fact, the splitting null was observed to be stress independent. The XY_8 model thus remains the only model consistent with the data. A $\sin^2\beta$ curve is superimposed on the data in Fig. 1(b) to show the quality of the fit.

Though the above symmetry arguments establish the validity of the XY_8 model, they do not provide all the details of the quadrupole splittings. In order to calculate the temperature and stress dependences of the splitting frequencies and the relation between splitting frequencies with S‖[110] and S‖[111], it is necessary to calculate R_8^{110} and R_8^{111}. The GBK model with energy levels determined by edge overlap integrals[6] is the starting point. The diagonalized XY_8 Hamiltonian matrix $\mathcal{H}_I$ is shown in Table II with elements labeled according to the transformation properties of the eigenstates. The center of gravity of the states has been adopted as the energy zero and the spacing between adjacent states designated Δ. The eigenstates in terms of the basis states ψ_n are tabulated in Table III.

The effect of stress is to modify the potential in which the Li^+ ion moves; the change is expressed as a stress Hamiltonian $\mathcal{H}_S$. Schawlow, Piksis, and Sugano[16] give expressions for linear stress Hamiltonians for

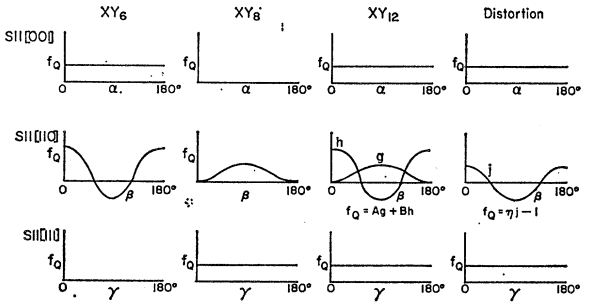

FIG. 5. Sketches of calculated stress-induced quadrupole splittings for XY_6, XY_8, XY_{12}, and distortion models with S‖[001], S‖[110], and S‖[111].

various stress directions as follows:

$$\mathcal{H}_S^{001}=S[(s_{11}+2s_{12})h(A_{1g})+2(s_{11}-s_{12})h_1(E_g)],$$

$$\mathcal{H}_S^{110}=S[(s_{11}+2s_{12})h(A_{1g})-(s_{11}-s_{12})h_1(E_g)+\tfrac{1}{2}s_{44}h_{xy}(T_{2g})],$$

$$\mathcal{H}_S^{111}=S[(s_{11}+2s_{12})h(A_{1g})+\tfrac{1}{3}s_{44}(h_{yz}(T_{2g})+h_{zx}(T_{2g})+h_{xy}(T_{2g}))],$$

where s_{11}, s_{12}, and s_{44} are independent elastic compliance coefficients and the $h_\mu(\Gamma^\nu)$ are functions of the Li^+ ion coordinate, which transform as labeled. The stress Hamiltonian matrix elements, $\langle\Psi_\mu(\Gamma^\nu)|\mathcal{H}_S|\Psi_\mu(\Gamma^\nu)\rangle$, are simplified by noting that contributions from terms of the form $\langle\psi_m|\mathcal{H}_S|\psi_n\rangle$, $n\neq m$, are small and may be neglected relative to terms of the form $\langle\psi_m|\mathcal{H}_S|\psi_m\rangle$. In this approximation only one independent parameter B, which comes from the T_{2g} terms in the Hamiltonian, appears in the stress Hamiltonian matrix elements. The A_{1g} terms give rise to a multiple of the diagonal unit matrix and thus serve only to shift the energy zero; since such a shift can have no observable effect, these A_{1g} matrix elements are omitted. The E_g terms make no contribution when overlap terms are ignored.

With the above approximation and omission the stress Hamiltonian matrix elements for S‖[001] are zero and those for S‖[110] and S‖[111] appear as tabulated in Table II.

The total Hamiltonian in the presence of stress is $\mathcal{H}=\mathcal{H}_I+\mathcal{H}_S$. For S‖[001] there is no perturbation and the eigenstates and energy levels remain those of the zero-stress case. This is the same result as the one obtained from symmetry arguments which led to the

TABLE III. XY_8 model eigenstates and energies at S = 0.

$\Psi(A_{1g})=(\frac{1}{8})^{1/2}(+\psi_a+\psi_b+\psi_c+\psi_d+\psi_e+\psi_f+\psi_g+\psi_h)$,	$E=-\frac{3}{2}\Delta$
$\Psi_{xy}(T_{2g})=(\frac{1}{8})^{1/2}(-\psi_a+\psi_b-\psi_c+\psi_d-\psi_e+\psi_f-\psi_g+\psi_h)$,	$E=\frac{1}{2}\Delta$
$\Psi_{yz}(T_{2g})=(\frac{1}{8})^{1/2}(-\psi_a+\psi_b+\psi_c-\psi_d+\psi_e-\psi_f-\psi_g+\psi_h)$,	$E=\frac{1}{2}\Delta$
$\Psi_{zx}(T_{2g})=(\frac{1}{8})^{1/2}(+\psi_a+\psi_b-\psi_c-\psi_d-\psi_e-\psi_f+\psi_g+\psi_h)$,	$E=\frac{1}{2}\Delta$
$\Psi_x(T_{1u})=(\frac{1}{8})^{1/2}(+\psi_a+\psi_b-\psi_c-\psi_d+\psi_e+\psi_f-\psi_g-\psi_h)$,	$E=-\frac{1}{2}\Delta$
$\Psi_y(T_{1u})=(\frac{1}{8})^{1/2}(-\psi_a+\psi_b+\psi_c-\psi_d-\psi_e+\psi_f+\psi_g-\psi_h)$,	$E=-\frac{1}{2}\Delta$
$\Psi_z(T_{1u})=(\frac{1}{8})^{1/2}(+\psi_a+\psi_b+\psi_c+\psi_d-\psi_e-\psi_f-\psi_g-\psi_h)$,	$E=-\frac{1}{2}\Delta$
$\Psi(A_{2u})=(\frac{1}{8})^{1/2}(-\psi_a+\psi_b-\psi_c+\psi_d+\psi_e-\psi_f+\psi_g-\psi_h)$,	$E=\frac{3}{2}\Delta$

[16] A. L. Schawlow, A. H. Piksis, and S. Sugano, Phys. Rev. 122, 1469 (1961).

TABLE IV. XY_8 model eigenstates and energies for S‖[110].

$$\Psi(A_{1g}\rightarrow A_{1g})=\left(\frac{1}{1+Z^2}\right)^{1/2}(\Psi(A_{1g})-Z\Psi_{xy}(T_{2g})),\quad E=-\tfrac{2}{3}\Delta-Y\Delta$$

$$\Psi(T_{2g}\rightarrow A_{1g})=\left(\frac{1}{1+Z^2}\right)^{1/2}(\Psi_{xy}(T_{2g})+Z\Psi(A_{1g})),\quad E=\tfrac{1}{2}\Delta+Y\Delta$$

$$\Psi(T_{2g}\rightarrow B_{1g})=(\tfrac{1}{2})^{1/2}\quad(\Psi_{yz}(T_{2g})-\Psi_{zx}(T_{2g})),\quad E=\tfrac{1}{2}\Delta-X\Delta$$

$$\Psi(T_{2g}\rightarrow B_{2g})=(\tfrac{1}{2})^{1/2}\quad(\Psi_{yz}(T_{2g})+\Psi_{zx}(T_{2g})),\quad E=\tfrac{1}{2}\Delta+X\Delta$$

$$\Psi(T_{1u}\rightarrow B_{1u})=(\tfrac{1}{2})^{1/2}\quad(\Psi_{x}(T_{1u})+\Psi_{y}(T_{1u})),\quad E=-\tfrac{1}{2}\Delta+X\Delta$$

$$\Psi(T_{1u}\rightarrow B_{2u})=(\tfrac{1}{2})^{1/2}\quad(\Psi_{x}(T_{1u})-\Psi_{y}(T_{1u})),\quad E=-\tfrac{1}{2}\Delta-X\Delta$$

$$\Psi(T_{1u}\rightarrow B_{3u})=\left(\frac{1}{1+Z^2}\right)^{1/2}(\Psi_{x}(T_{1u})-Z\Psi(A_{2u})),\quad E=-\tfrac{1}{2}\Delta-Y\Delta$$

$$\Psi(A_{2u}\rightarrow B_{3u})=\left(\frac{1}{1+Z^2}\right)^{1/2}(\Psi(A_{2u})+Z\Psi_{z}(T_{1u})),\quad E=\tfrac{3}{2}\Delta+Y\Delta$$

$$X=(B/\Delta)S,\quad Y=((X^2+1)^{1/2}-1),\quad Z=Y/X$$

conclusion that for S‖[001] there is no quadrupole splitting. In Fig. 7 of Ref. 6 GBK show the degeneracy of the T_{1u} and T_{2g} states lifted by stress parallel to [001]; this is because GBK's calculation includes effects due to the $\langle\psi_m|\mathcal{H}_S^{001}|\psi_n\rangle$, $m\neq n$, terms which have been ignored here. Stresses parallel to [110] and [111] mix the states. Exact eigenstate and energy solutions to the S‖[110] and S‖[111] problems are tabulated in Tables IV and V; the energy solutions are plotted in Figs. 6 and 7. All results are written in terms of a dimensionless stress parameter $X=(B/\Delta)S$, where

$$B=\tfrac{1}{2}S_{44}\int\Psi^*(A_{1g})h_{xy}(T_{2g})\Psi_{xy}(T_{2g})d^3x.$$

These results yield the $c_{nu}(\Gamma^\nu)$ as a function of stress direction and X. Equations (6) and (8) now yield R_8^{110} as a function f X, Δ, and temperature T, and Eqs. (6) and (9) yield R_8^{111} as a function of X, Δ, and T. The parameter R_8^{110} is independent of the sign of X but R_8^{111} is not.

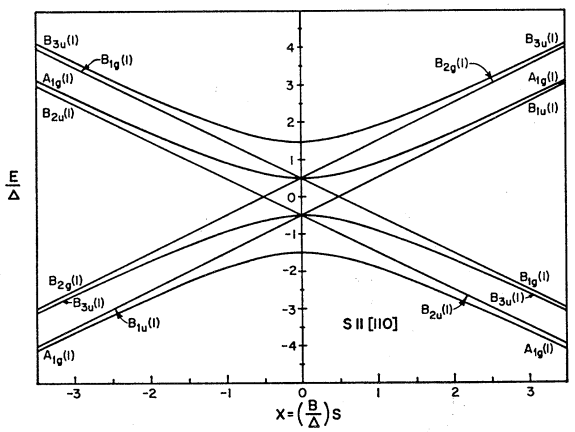

FIG. 6. Energy-level diagram for XY_8 model with S‖[110].

The stress and temperature-dependence data of Fig. 3 can now be fitted as follows. First choose a value for Δ, leaving R_8^{110} dependent only on X and T. Now note that for S‖[110] and $\beta=90°$, $f_Q=\frac{1}{4}(e^2Qq_8/h)R_8^{110}$, so that f_Q depends linearly on R_8^{110} through the unknown parameter $\frac{1}{4}(e^2Qq_8/h)$. Also, since $X=(B/\Delta)S$, X depends linearly on S through the unknown parameter (B/Δ). Thus for a given temperature a theoretical $\log R_8^{110}$-versus-$\log X$ plot should fit an experimental $\log f_Q$-versus-$\log S$ plot when the two are superimposed so that $\log X=\log S+\log(B/\Delta)$ and $\log f_Q=\log R_8^{110}+\log\frac{1}{4}(e^2Qq_8/h)$. The results of such a fit assuming the Harrison-Peressini-Pohl[11] value of Δ for the Li^7 impurity, $\Delta=0.82$ cm^{-1}, is shown in Fig. 3; in adjusting the fit particular attention was paid to the high stress points where the experimental uncertainty was least. The results of the fit are $B/\Delta=\pm0.0100\pm0.0006$ bar^{-1} and $\frac{1}{4}(e^2Qq_8/h)=17.8$ kHz so that $B=\pm0.0082\pm0.0005$ cm^{-1} bar^{-1} and $(e^2Qq_8/h)=71\pm3$ kHz. The $\pm$ on the value of B reflects the fact that since R_8^{110} is independent of B's sign, B's sign is not determined. Fits to the low stress data were improved slightly by varying Δ downward, but B changes less than 5% and (e^2Qq_8/h) changes less than 2% using best fits with Δ between 0.6 cm^{-1} and 0.9 cm^{-1}. The departure from perfect fit is attributed to experimental error in the 3.24 K, 287 bar point and to shortcomings in the model for the low stress points.

All the parameters necessary to calculate the quadrupole splitting induced by S‖[111] are now available. The result depends on the sign of B. The parameter R_8^{111} is calculated using $\Delta=0.82$ cm^{-1}, $T=1.30$ K, $S=-287$ bar (negative because of compressive stress), and first $B=+0.0082$ cm^{-1} bar^{-1}, then $B=-0.0082$ cm^{-1} bar^{-1}. The equation $f_Q=\frac{1}{4}(e^2Qq_8/h)R_8^{111}$ with $\frac{1}{4}(e^2Qq_8/h)=17.8$ kHz is then used to obtain f_Q. The result is $f_Q=8.75$ kHz for positive B and 4.37 kHz for negative B. These values are plotted as lines in Fig. 1(c). Insofar as the observed splitting, $f_Q=5.5\pm0.5$ kHz, is closer to 4.37 kHz than to 8.75 kHz the sign of B can be said to be negative. This implies that upon compression parallel to the [110] axis the Li^+ ion moves from wells b, d, f, and h into wells a, c, e, and g; upon compression parallel to the [111] axis the Li^+ ion moves from wells b and h into wells a, c, d, e, f, and g.

In Fig. 3 the theoretical curves lie lower than the experimental points. Comparing the S‖[110] and S‖[111] stress Hamiltonians demonstrates the equivalence of stress parallel to [111] to simultaneous stresses of two-thirds the magnitude parallel to [110], [011], and [101]. Thus perhaps the S‖[111] calculation suffers from the same errors as does the S‖[110] calculation at low stress. Upwards correction of the calculation would improve the negative B fit but would worsen the positive B fit; this offers encouragement that the choice of the negative sign for B is correct.

TABLE V. XY_8 model eigenstates and energies for S‖[111].

$$\Psi(A_{1g}\rightarrow A_{1g})=\left(\frac{1}{1+V_g^2}\right)^{1/2}[\Psi(A_{1g})-V_g(\tfrac{1}{3})^{1/2}(\Psi_{yz}(T_{2g})+\Psi_{zx}(T_{2g})+\Psi_{xy}(T_{2g}))], \qquad E=-\tfrac{3}{2}\Delta+[U+1-((U+1)^2+3U^2)^{1/2}]\Delta$$

$$\Psi(T_{2g}\rightarrow A_{1g})=\left(\frac{1}{1+V_g^2}\right)^{1/2}[(\tfrac{1}{3})^{1/2}(\Psi_{yz}(T_{2g})+\Psi_{zx}(T_{2g})+\Psi_{xy}(T_{2g}))+V_g\Psi(A_{1g})], \qquad E=\tfrac{1}{2}\Delta+[U-1+((U+1)^2+3U^2)^{1/2}]\Delta$$

$$\Psi(T_{2g}\rightarrow E_g)=(\tfrac{1}{6})^{1/2}(\Psi_{yz}(T_{2g})+\Psi_{zx}(T_{2g})-2\Psi_{xy}(T_{2g})), \qquad E=\tfrac{1}{2}\Delta-U\Delta$$

$$\Psi(T_{2g}\rightarrow E_g)=(\tfrac{1}{2})^{1/2}(\Psi_{yz}(T_{2g})-\Psi_{zx}(T_{2g})), \qquad E=\tfrac{1}{2}\Delta-U\Delta$$

$$\Psi(T_{1u}\rightarrow E_u)=(\tfrac{1}{6})^{1/2}(\Psi_x(T_{1u})+\Psi_y(T_{1u})-2\Psi_z(T_{1u})), \qquad E=-\tfrac{1}{2}\Delta-U\Delta$$

$$\Psi(T_{1u}\rightarrow E_u)=(\tfrac{1}{2})^{1/2}(\Psi_x(T_{1u})-\Psi_y(T_{1u})), \qquad E=-\tfrac{1}{2}\Delta-U\Delta$$

$$\Psi(T_{1u}\rightarrow A_{2u})=\left(\frac{1}{1+V_u^2}\right)^{1/2}[(\tfrac{1}{3})^{1/2}(\Psi_x(T_{1u})+\Psi_y(T_{1u})+\Psi_z(T_{1u}))-V_u\Psi(A_{2u})], \qquad E=-\tfrac{1}{2}\Delta+[U+1-((U-1)^2+3U^2)^{1/2}]\Delta$$

$$\Psi(A_{2u}\rightarrow A_{2u})=\left(\frac{1}{1+V_u^2}\right)^{1/2}[\Psi(A_{2u})+V_u(\tfrac{1}{3})^{1/2}(\Psi_x(T_{1u})+\Psi_y(T_{1u})+\Psi_z(T_{1u}))], \qquad E=\tfrac{3}{2}\Delta+[U-1+((U-1)^2+3U^2)^{1/2}]\Delta$$

$$U=\tfrac{2}{3}X=\tfrac{2}{3}(B/\Delta)S, \quad V_g=\frac{-U-1+((U+1)^2+3U^2)^{1/2}}{(3)^{1/2}U}, \quad V_u=\frac{U-1+((U-1)^2+3U^2)^{1/2}}{(3)^{1/2}U}$$

Imperfections in these fits are not surprising in light of the simplicity of the model used. Indeed, it is the simplest model that can be constructed; only the variables necessary to produce a nonzero quadrupole splitting are included, everything else is assumed zero or constant. Obvious improvements in the model would include: (i) allowance for variation of Δ with stress and temperature, (ii) consideration of the broadening of the levels by their finite lifetime, (iii) inclusion of other than edge overlap integrals in the determination of the zero stress energy levels, (iv) retention of the effects of overlap integrals in the stress Hamiltonian, (v) inclusion of terms of higher order in S in the stress Hamiltonian, and (vi) retention of overlap integrals in the derivation of Eq. (5).

The narrowing of the sidebands when a large stress is applied parallel to [110] at $\beta=90°$ can be explained as follows: The only terms in the stress Hamiltonians which have any effect on the quadrupole splittings are the three T_{2g} terms, $h_{xy}(T_{2g})$, $h_{yz}(T_{2g})$, and $h_{zx}(T_{2g})$; these terms are associated with stresses in the [110], [011], and [101] directions, respectively. The quadrupole splittings associated with $h_{xy}(T_{2g})$ were calculated when the S‖[110] case was treated and found to be proportional to

$$3\cos^2\theta-1+\sin^2\theta\cos2\varphi,$$

where θ and φ are polar coordinates of the magnetic field defined in a coordinate system: $\hat{x}\|[001]$, $\hat{y}\|[1\bar{1}0]$, $\hat{z}\|[110]$. This function is zero and thus the quadrupole splitting is zero when the magnetic field lies in either the (100) plane or the (010) plane. Likewise, the splitting due to $h_{yz}(T_{2g})$ is zero when the magnetic field lies in either the (010) plane or the (001) plane and the splitting due to $h_{zx}(T_{2g})$ is zero when the magnetic field lies in either the (001) plane or the (100) plane. Random stress is certainly present in the crystal and thus the three terms $h_{xy}(T_{2g})$, $h_{yz}(T_{2g})$, and $h_{zx}(T_{2g})$ are present in random strengths in the Hamiltonian of the impurity site before external stress is applied. However, when stress parallel to [110] is applied, large amounts of $h_{xy}(T_{2g})$ are introduced into the total Hamiltonian. From Fig. 3 it is clear that the quadrupole splitting due to $h_{xy}(T_{2g})$ is nearly saturated; that is, a little more or less stress parallel to [110] causes little change in the quadrupole splitting. Thus the $h_{xy}(T_{2g})$ random stress terms have little effect on the quadrupole splittings. The $h_{yz}(T_{2g})$ and $h_{zx}(T_{2g})$ terms cause no splitting when the magnetic field is in the (001) plane, as it is when it is parallel to [110]. Thus for large stresses parallel to [110] with the magnetic field parallel to [1$\bar{1}$0], random stresses have no effect on the quadrupole splitting; this accounts for the narrow sidebands observed. As the magnetic field is rotated away from [1$\bar{1}$0], however, $h_{yz}(T_{2g})$ and $h_{zx}(T_{2g})$ come into play and the sidebands broaden

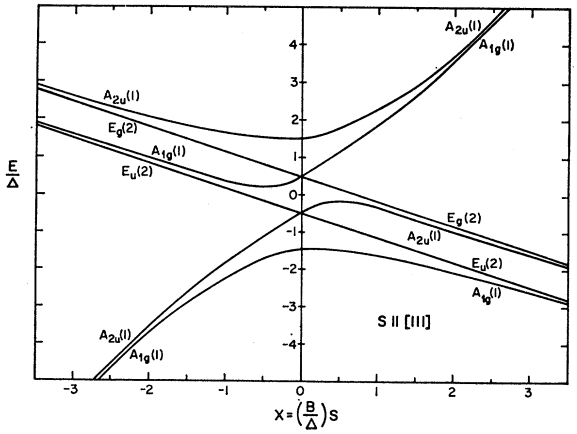

FIG. 7. Energy-level diagram for XY_8 model with S‖[111].

TABLE VI. Comparison of experimental results and point-ion calculations.

	Interionic distance used (Å)	Appropriate temperature (K)	Off-center direction	Off-center distance to potential minimum (Å)	e^2Qq/h[a] (kHz)
Present experiment	3.117	1–4	⟨111⟩		71±3
Quigley and Das	3.147	300	⟨111⟩	0.60	119.6
calculation[b,c]	3.117	4	⟨111⟩	0.44	85.
Wilson and Blume	3.147	300	⟨111⟩	1.16	300.4
calculation[d,c]				0.55	62.68[e]

[a] Actually $e^2Q(1-\gamma_\infty)q/h$ in calculations.
[b] References 9 and 17.
[c] Note that Quigley and Das and Wilson and Blume use different values of the Li^7 quadrupole moment, $|Q|=0.050$ b and $|Q|=0.042$ b, respectively.
[d] Reference 18.
[e] Not at calculated potential minimum.

because of random stress. Also, when the stress applied parallel to [110] is decreased the stress splitting is no longer saturated and $h_{xy}(T_{2g})$ random stresses broaden the sidebands. When $\mathbf{S}\|[111]$ the conditions for sideband narrowing never exist and the sidebands will always be broadened by random stress. This is exactly what was observed.

The magnitude of the T_{2g} random stresses can be obtained from the linewidths measured with the magnetic field parallel to $[1\bar{1}0]$. The difference of 0.64 kHz^2 between the second moments of the zero-stress line and the central line with quadrupole sidebands removed is due to random stress. It was shown in the previous paragraph that only the $h_{xy}(T_{2g})$ stress terms contribute to this width. The effect of the $h_{xy}(T_{2g})$ stress terms has been calculated; at low stresses the $T=1.30$ K curve of Fig. 3 goes to $f_Q/S=0.14$ kHz/bar. Thus the rms stress can be calculated:

$$(S_{AV}^2)^{1/2}=0.14^{-1}(f_Q^2)^{1/2}=5.7 \text{ bar}.$$

Thus the rms T_{2g} stress is 5.7 bar. It is reasonable to assume that the $T_{2g}(xy)$ and $T_{2g}(zx)$ rms stresses are identical. The A_{1g} and E_g random stresses remain unmeasured.

V. CONCLUSIONS

The GBK[6] LCAO XY_8 model extended to account for uniaxial stress predicts the stress induced Li^7 NMR quadrupole splitting patterns observed in KCl:Li^+. In particular, the splitting patterns obtained with the magnetic field rotated in a plane perpendicular to stresses parallel to [001], [110], and [111] are in agreement with calculations using the XY_8 model. On the other hand, the XY_6, XY_{12}, and distortion models predict splitting patterns quite different from those observed. This is taken as unambiguous verification of the appropriateness of the XY_8 model. Further, data on quadrupole splitting frequencies as a function of temperature and stress magnitude are reasonably well fitted by the theory; the fit yields the parameter which describes the response of the impurity site to stress. The strength of the EFG which the Li^7 nucleus experiences when it is off center is also determined. The result is a fairly detailed model of the impurity dynamics and Li^7 quadrupole interactions in KCl:Li^+. Refinements and extensions of the model are certainly possible, but its quantitative success along with its simplicity commend the model as a good first approximation.

Comparisons of the experimental results with the point-ion calculations of Quigley and Das[9,17] and of Wilson and Blume[18] are shown in Table VI. Note that values of e^2Qq/h calculated for the smaller Li^+ ion displacements are in closer agreement with the experimental value. Whether or not the experimental value may be used as a measure of the Li^+ ion's displacement depends upon the accuracy of the calculations and on the validity of the assumptions made in deriving the experimental value. It should be pointed out that the experimental value of e^2Qq/h represents an average of EFG near the well minimum whereas the calculated values are of EFG's at a single point.

The above conclusions demonstrate the usefulness of NMR as a tool for the study of the lattice dynamics of substitional defects. Work is now underway to extend this usefulness with pulsed NMR measurements of the Li^7 spin-lattice relaxation time and inhomogeneous quadrupole interactions in KCl:Li^+.

ACKNOWLEDGMENTS

The help of P. Peressini in obtaining and handling KCl:Li^+ crystals and many helpful discussions of the experimental aspects of this problem with D. Miyoshi are gratefully acknowledged.

[17] R. J. Quigley and T. P. Das, Phys. Rev. **177**, 1340 (1969); and (private communication).
[18] W. D. Wilson and M. Blume, J. Phys. Chem. Solids **29**, 1167 (1968).